Creep Resistance and Structure of 10% Cr–3% Co–2% W–0.29% Cu–0.17% Re Steel with Low Nitrogen and High Boron Contents for Unit Components of Coal Power Plants

A. Fedoseeva

Belgorod State National Research University, Belgorod, 308015 Russia
e-mail: fedoseeva@bsu.edu.ru, alexandra_plot@mail.ru

Abstract—The creep resistance and structure of 10% Cr–3% Co–2% W–0.29% Cu–0.17% Re steel with 0.1% carbon, low nitrogen content and high boron content were investigated by creep rupture testing at a temperature of 650°C and stresses from 200 to 100 MPa applied in 20-MPa increments. For comparison, 9% Cr steel with 0.1% carbon, 0.05% nitrogen, and 0.005% boron was considered. The steels were subjected to preliminary heat treatment including normalizing at 1050°C for 1 hour, tempering at 750–770°C for 3 hours, and cooling in air. The structures of both heat-treated steels exhibited martensite laths with boundaries pinned by $M_{23}C_6$ carbides, and the rearrangement of dislocations was retarded by MX particles. A significant difference between 10% Cr and 9% Cr steels was the presence of fine $M_{23}C_6$ carbide particles characterized by orientational relationships with the ferrite matrix and MX carbonitrides, whose volume fraction was 6 times lower. Short-term tensile tests at room temperature showed no differences between the steels, while the creep rupture strength of 10% Cr steel was 13% higher than for 9% Cr steel. The creep deformation mechanism of the steels was also different. Structural analysis of 10% Cr steel after creep tests revealed no substantial changes in its lath structure: the lath width increased by only 58% and the dislocation density was reduced by a factor of 2. Comparison with 9% Cr steel showed that the good structural stability of 10% Cr steel during creep is caused by the high coarsening resistance of second phase particles, whose coarsening rate is 1-2 orders of magnitude lower than that in 9% Cr steel.

Keywords: heat-resistant martensitic steels, alloying, creep resistance, strength, strengthening mechanisms, structure, particle coarsening

1. INTRODUCTION

Transition to a new generation of coal-fired power plant units operating at ultra-supercritical steam parameters requires the development of new structural materials [1]. The main task is to create new boiler materials with desired performance under ultra-supercritical steam conditions. The key requirements for modern materials for ultra-supercritical steam boilers, steam pipelines and steam turbine blades are a long-term strength of at least 100 MPa at a temperature of 650°C, room temperature impact strength of at least 59 J/cm², and room temperature yield strength and tensile strength of not less than 500 and 700 MPa, respectively [1, 2]. High-chromium martensitic steels are promising candidates for the manufacture of boiler elements, steam pipelines, steam heaters, and steam turbine elements for power units operating with ultra-supercritical steam. These steels have good mechanical characteristics, a low coefficient of thermal expansion [1, 3], and relatively low cost compared to austenitic steels and nickel alloys. However, their creep resistance is insufficiently high at temperatures of 650°C and above [4–6]. The creep resistance can be enhanced by changing alloying parameters and selecting thermal or thermomechanical treatments [1, 6]. Currently, the most significant alloying aspects in the development of high-chromium martensitic steels are the following:

– balance of C, V, Nb and/or Ta and N contents to obtain stable MX particles,

– increase in the content of Mo and W for solid solution and dispersion strengthening due to $M_{23}C_6$ and Laves phase,

– addition of Co, Cu and Mn to suppress δ-ferrite,

– addition of Cu for the nucleation of Laves phase particles on copper particles,

– alloying with B to stabilize $M_{23}C_6$.

The structure of high-chromium steels is a complex hierarchical system in which the original austenite grains are divided into packets of blocks consisting of martensite laths, with a high density of dislocations within the laths [7]. The high dislocation density leads to a nonequilibrium structure and creates large driving forces for recrystallization during heating [1, 5].

The main contribution to the stabilization of the nonequilibrium troostite-martensite structure during creep is made by a solid solution with elements such as cobalt, tungsten and molybdenum, which markedly reduce the diffusion rate, and particles of $M_{23}C_6$ carbides, MX carbonitrides and $(Fe_2(W, Mo))$ Laves phase. The decrease in the diffusion rate at high temperatures inhibits the redistribution of dislocations due to creep. This in turn causes a significant reduction in the rate of transformation of martensite lath boundaries with a misorientation of ≤2°, which are sources of long-range elastic stress fields, into subgrain boundaries, in which long-range stress fields are either absent or insignificant [1, 5, 8]. In addition, the presence of cobalt, tungsten and molybdenum in the solid solution and especially boron along the structural boundaries suppresses the coarsening of $M_{23}C_6$ carbides and thus also prevents subgrain structure formation [3, 8–10]. However, the W and Mo content in the solid solution exceeds the equilibrium value at operating temperatures of ~630–650°C, due to which W and Mo are segregated from the solid solution to equilibrium concentrations with the formation of $Fe_2(W, Mo)$ Laves phase during long-term aging and creep [11, 12]. This enhances the dislocation creep and leads to $M_{23}C_6$ carbide coarsening, due to which the lath structure of tempered troostite transforms into a subgrain structure [6, 8]. As a result of this transformation, high-chromium steels lose their unique creep resistance, and their creep rupture strength sharply increases with the transition from short- to long-term creep [13]. It should be noted that the depletion of the W–Mo solid solution and the $M_{23}C_6$ carbide coarsening are interrelated. The deple-

tion of W and Mo substitutional elements in the solid solution inevitably accelerates diffusion processes, including particle coarsening during long-term aging and creep. Additional alloying with boron, which reduces the interfacial energy of carbides, can retard the coarsening of $M_{23}C_6$ carbides [1, 14–16], but it cannot prevent the Laves phase coarsening and dislocation creep acceleration due to solid solution depletion in tungsten and molybdenum. Rhenium was supposed to help solve this problem by increasing the solubility of tungsten in the solid solution at 650°C [17, 18]. However, later studies did not confirm this hypothesis [19]. On the other hand, it was found that adding rhenium and increasing tungsten content to 3% ensures the coherency of particle/matrix interfaces and reduces the diffusion rate, preventing the dissolution of $M_{23}C_6$ carbide and Laves phase chains along martensite lath boundaries during creep. These chains stabilize the troostite-martensite lath structure during creep for ~11 000 h under high applied stress [20]. This work continues a series of studies of Re-containing 10% Cr steels, seeking to increase their creep resistance and suppress structural degradation during creep [6, 19–22]. Here we investigate the structure and creep resistance of Re-containing 10% Cr steel with low nitrogen content and high boron content. The aim is to identify the specific features that provide high creep resistance compared to 9% Cr steel with 0.1% carbon, 0.05% nitrogen and 0.005% boron, without rhenium.

2. MATERIAL AND METHODS

Material for the investigation was 10% Cr steel smelted in a vacuum induction furnace. For comparison, 9% Cr steel was used, whose structure and properties are described in detail in [8]. The chemical compositions of the steels were determined using optical emission spectrometry (FOUNDRY-MASTER UVR) and gas analysis methods (METEC-300/METEC-600) and are presented in Table 1.

Both steels were subjected to preliminary homogenization annealing at a temperature of 1150°C for 16 hours, followed by bidirectional forging at the same temperature to a true strain of ~1 and cooling in air. Then both steels were normalized at a tempera-

Table 1. Chemical composition of the studied steels (in wt %)

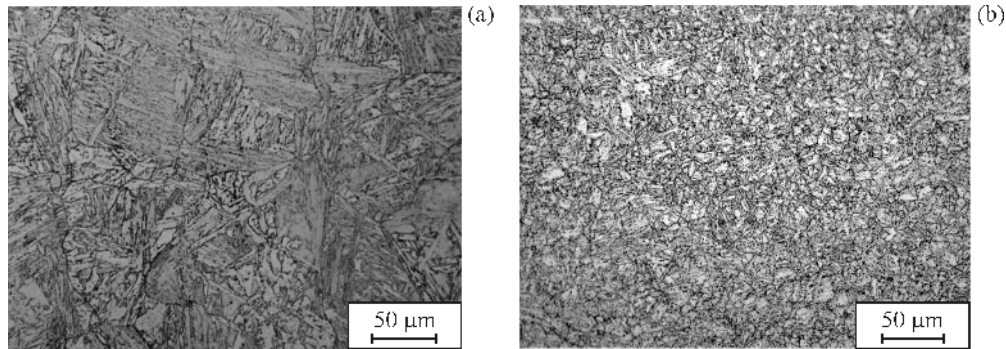|	Fe	C	Cr	Co	W	Mo	V	Nb	Cu	Re	N	B	Ni	Si	Mn	Al
10% Cr	bal.	0.1	9.4	3.1	2.1	0.6	0.16	0.05	0.29	0.17	0.001	0.015	0.2	0.1	0.03	0.04
9% Cr	bal.	0.1	9.1	3.0	1.8	0.5	0.23	0.05	–	–	0.05	0.05	0.2	0.1	0.2	0.01

Fig. 1. Optical metallographic images of the macrostructure of the studied 10% Cr steel (a) and 9% Cr steel for comparison (b) after heat treatment.

ture of 1050°C for 1 hour, cooled in air, and tempered at a temperature of 750°C for 9% Cr steel and 770°C for 10% Cr steel for 3 hours with air cooling. The higher tempering temperature of 10% Cr steel was chosen to ensure good impact toughness.

Uniaxial tensile tests were conducted at room temperature on 3 flat specimens with a gauge length of 27 mm and a cross section of 7×3 mm^2 with a strain rate of 10^{-3} s^{-1} using an Instron 5882 universal testing machine in accordance with GOST 1497-84. Hardness measurements were carried out at room temperature on a plane-parallel sample with dimensions of $10 \times 15 \times 15$ mm with a ground working surface using a Wolpert 3000BLD digital Brinell hardness tester in accordance with GOST 9012-59 (ball diameter $D = 5$ mm, load 750 kgf). Long-term creep rupture tests were performed on flat specimens with a gauge length of 25 mm and a cross section of 7×3 mm^2 at a temperature of 650°C and nominal stresses from 200 to 100 MPa in 20-MPa increments to failure using an ATS 2330 lever-arm testing machine according to ASTM E139-00 standard procedure.

The structure of the material was examined by optical microscopy (Olympus GX70), transmission electron microscopy (JEOL-2100 with an INCA energy dispersive X-ray spectrometer), and scanning electron microscopy (Quanta 600 with an EBSD detector). Optical metallography was performed on samples etched in an aqueous solution of 2% nitric acid and 1% hydrofluoric acid for 30 s. TEM and SEM studies were performed on thin foils electrolytically thinned in a solution of 10% perchloric acid in acetic acid at a voltage of 23 V using a TenuPol-5 device. The size of the original austenite grains, the width of martensite laths, and the distance between high-angle boundaries were determined by the random secant

method. The dislocation density was measured as the number of emergence points on the upper and lower surfaces of the foil. Particle type was determined by a combination of methods for measuring selected area electron diffraction patterns and by TEM analysis of the local chemical composition of particles. The volume fractions of equilibrium phases were calculated by mathematical modeling with Thermo-Calc software (Version 5.0.4 75) using TCFE7 thermodynamic database for steels. More information about the methods used can be found elsewhere [6, 8, 13, 19–22].

Table 2. Structural parameters of 10% Cr and 9% Cr steels after heat treatment

Structural parameters	10% Cr steel	9% Cr steel
Original austenite grain size, μm	65 ± 5	10 ± 5
Fraction of δ-ferrite, %	0	0
Lath size, nm	380 ± 30	380 ± 30
Dislocation density, 10^{14} m^{-2}	1.44 ± 0.1	2.0 ± 0.1
HAB spacing, μm	2.60	1.76
Fraction of HAB, %	52	63
Fraction of LAB, %	48	37
Average size of M$_{23}$C$_6$, nm	70 ± 7	90 ± 7
Volume fraction* of M$_{23}$C$_6$, %	2.35	2.27
Average size of W-rich particles, nm	40 ± 4	–
Average size of M(C, N), nm	30 ± 3	40 ± 3
Volume fraction* of M(C, N), %	0.054	0.34
Particle density at HAB, μm^{-1}	5.69	1.41
Particle density at LAB, μm^{-1}	2.01	0.94

* Calculated using Thermo-Calc software. HAB—high-angle boundaries, LAB—low-angle boundaries.
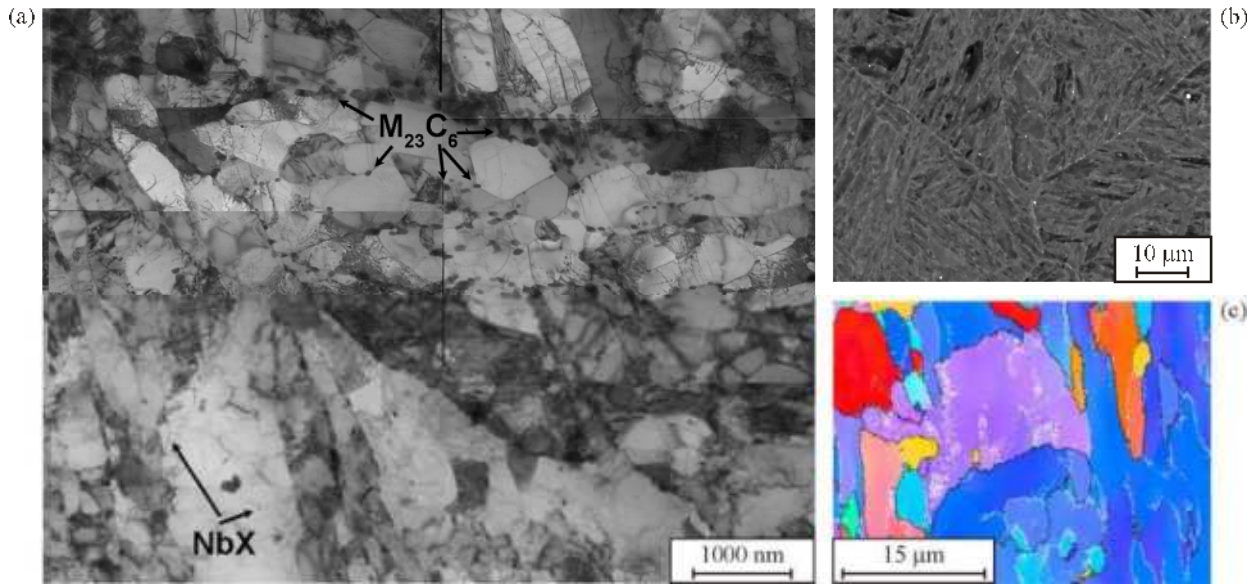
Fig. 2. Micrographs of heat-treated 10% Cr steel, TEM (a), SEM (b), EBSD (c) on thin foils (color online).

3. RESULTS AND DISCUSSION

3.1. Initial State after Heat treatment

Optical metallographic macrostructures of the studied 10% Cr steel and 9% Cr steel for comparison after heat treatment are presented in Fig. 1. The original austenite grain size in 10% Cr steel was about 60 μm, which is much larger than in 9% Cr steel with a standard content of carbon, nitrogen and boron (Table 1). δ-ferrite was not detected in both steels (Fig. 1, Table 1).

It is known that the original austenite grain size is determined by the content of MX carbonitrides, which remain undissolved during high-temperature austenitization of steel and produce retarding forces of recrystallization [23]. A significant decrease in the nitrogen content in 10% Cr steel reduces the propor-

tion of MX carbonitrides (Table 2), and as a result the original austenite grain size increases.

TEM, SEM and EBSD microstructures of heat-treated 10% Cr steel are shown in Fig. 2. The size and misorientation distributions of subgrains/grains are given in Fig. 3. It can be seen that heat treatment of 10% Cr steel causes the formation of a uniform tempered troostite structure (Fig. 2c). The average transverse size of martensite laths is 380 ± 30 nm in both steels (Table 2). The dislocation density within the laths is high in both steels (Table 2). SEM microstructural analysis of 10% Cr steel foils (Fig. 2b) revealed a small amount of large tungsten-rich particles, presumably W_2B [24], which remained undissolved during normalization. EBSD analysis showed (Fig. 2c) that the fraction of high- and low-angle
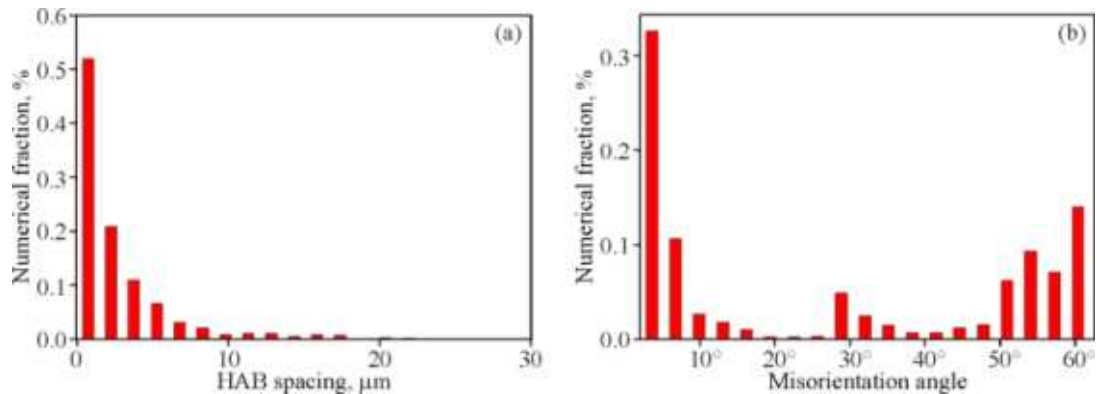

Fig. 3. Size distribution of grains with high-angle grain boundaries (a) and misorientation distribution of subgrains/grains (b) obtained from EBSD measurements on 10% Cr steel foil.
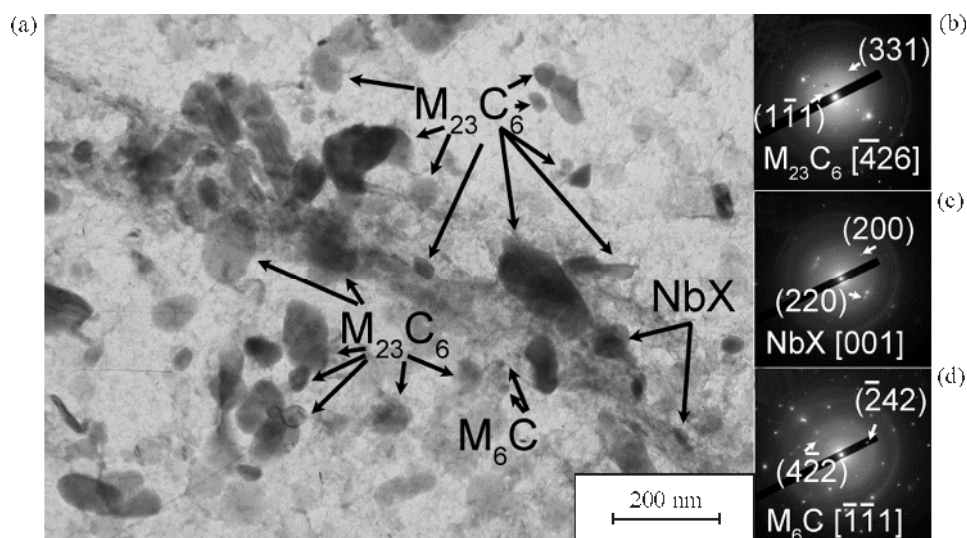
Fig. 4. Image showing second phase particles in 10% Cr steel (a) with selected area electron diffraction patterns for $M_{23}C_6$ carbides (b), NbX carbonitrides (c) and M_6C carbides (d) after heat treatment. TEM micrographs of carbon replicas.

boundaries in 10% Cr steel was 52 and 4%, respectively, and the average distance between high-angle boundaries was 2.6 μm (Fig. 3a, Table 2). In contrast, 9% Cr showed a 21% higher fraction of high-angle boundaries and a 23% lower fraction of low-angle boundaries, due to which the high-angle boundary spacing was 32% smaller (Table 2). The subgrain/grain misorientation distribution in 10% Cr steel (Fig. 3b) was binary with peaks at 2°–5° and 55°–60°, corresponding to martensite lath boundaries and original austenite grain boundaries, respectively. Note that many dislocation boundaries of martensite laths are misoriented by less than 2°, which is not taken into account in EBSD measurements. A small peak was also observed in 10% Cr steel at a misorientation of about 30° (Fig. 3b), which corresponds to the packet boundaries.

The chemical composition of the matrix in 10% Cr steel was determined by averaging ten data sets collected for the ferrite solid solution at different points of the foil away from particles using an INCA energy dispersive X-ray spectrometer attached to the JEOL-2100 transmission electron microscope. The determined chemical composition corresponds (in wt %) to 84% Fe–9% Cr–3.6% Co–2.45% W–0.57% Mo–0.2% Re–0.2% V. Thus it is clear that the content of substitutional elements such as cobalt, tungsten, molybdenum and rhenium, as well as vanadium as the carbide-forming element, practically does not change taking into account the measurement error, which indicates that these elements are retained in the ferrite solid solution. However, the chromium content de-

creases from 9.4 to 9.0% due to the precipitation of chromium-containing phases/phase, and niobium is completely removed from the solid solution due to the precipitation of niobium-containing phases/phase.

Analysis of replicas (Fig. 4) showed that heat treatment promotes the precipitation of chromium-rich $M_{23}C_6$ carbides (Fig. 4b), niobium-rich MX carbonitrides (Fig. 4c), and a very small amount of tungsten-rich M_6C carbides (Fig. 4d). $M_{23}C_6$ carbides and MX carbonitrides were also found in 9% Cr steel [6, 8], but the size of $M_{23}C_6$ particles was much larger and their number density at both high- and low-angle lath boundaries was much lower, while the volume density of MX carbonitrides was 6 times higher (Table 2).

TEM structural studies of foils and carbon replicas showed that $M_{23}C_6$ carbides are the dominant phase in both 9% and 10% Cr steels, where they are mainly located along the boundaries of the original austenite grains, packets, blocks and martensite laths (Figs. 2a and 4a). These particles are enriched in Cr, Fe and W in both steels, and their average chemical composition corresponds (in wt %) to 43% Cr–17% Fe–0.5% Mo–40% W in 10% Cr steel.

Figure 5 shows size distribution histograms of $M_{23}C_6$ particles in the structure of tempered troostite in 10% Cr and 9% Cr steels after heat treatment.

As seen from Fig. 5, 10% Cr steel is characterized by the small size of $M_{23}C_6$ carbides, which is due to the partial replacement of carbon atoms with boron atoms and the formation of $M_{23}(C, B)_6$ particles during tempering [6, 14, 16]. Thus, the main peak of the
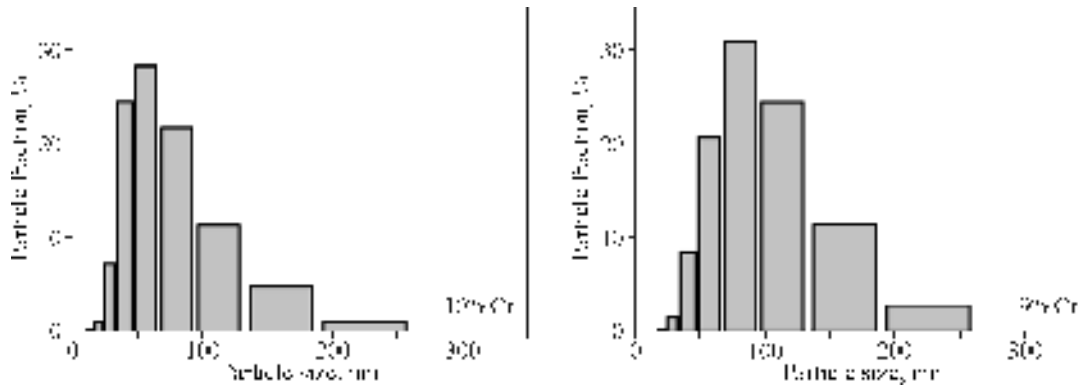
Fig. 5. Distribution of $M_{23}C_6$ carbide particles in the structure of tempered troostite in 10% Cr (a) and 9% Cr steels (b) after heat treatment.

$M_{23}C_6$ particle size distribution in 10% Cr steel corresponds to particle sizes from 50 to 75 nm, with more than 80% of particles belonging to the size range up to 100 nm (Fig. 5a). The fraction of very large particles with sizes greater than 200 nm does not exceed 1% (Fig. 5a). On the contrary, for 9% Cr steel the main peak of the $M_{23}C_6$ particle size distribution is shifted towards larger sizes compared to 10% Cr steel and lies in the range from 75 to 100 nm (Fig. 5b). The fraction of particles with sizes up to 100 nm is 60%. Moreover, the fraction of particles with sizes from 100 to 200 nm is 2.3 times greater than in 10% Cr steel (Fig. 5b). The fraction of very large particles with sizes greater than 200 nm is 3% (Fig. 5b). The refinement of $M_{23}C_6$ carbides in 10% Cr steel results in their higher number density at high- and low-angle

grain boundaries with the same volume fraction of these particles in 9% Cr and 10% Cr steels (Table 2).

Analysis of heat-treated 10% Cr steel revealed orientation relationships between $M_{23}C_6$ carbides and the ferrite matrix at low-angle lath boundaries (Fig. 6), corresponding to the well-known Pitsch and Kurdyumov–Sachs relationships [25].

The obtained orientation relationships between $M_{23}C_6$ and the ferrite matrix of heat-treated 10% Cr steel indicate that these particles are strongly associated with the ferrite matrix. $M_{23}C_6$ carbides can effectively inhibit the migration of low-angle lath boundaries. Our previous study of rhenium-containing 10% Cr steel showed that $M_{23}C_6$ particles at martensite lath boundaries retain their orientation relationships for at least 10 000 hours of creep and are the
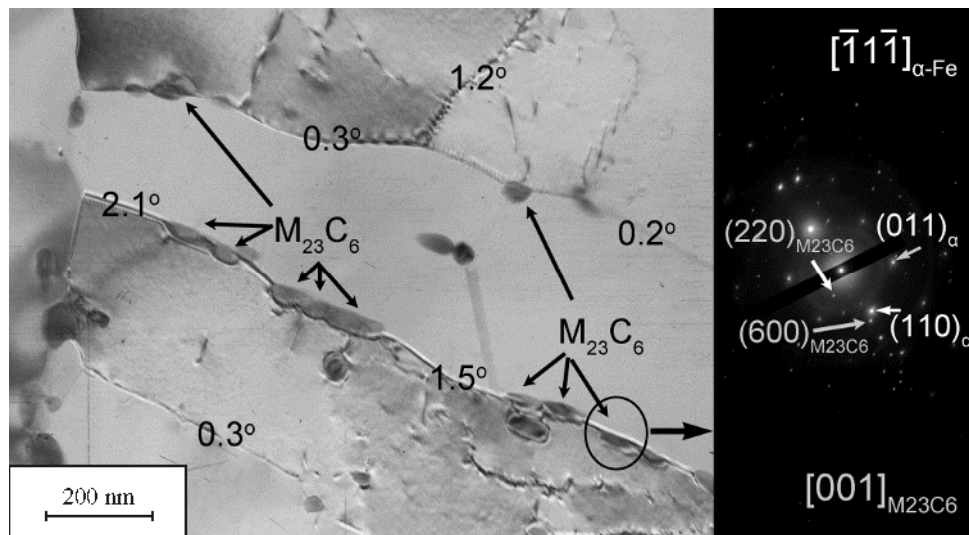

Fig. 6. Image showing $M_{23}C_6$ carbides at low-angle martensite lath boundaries (numbers indicate boundary misorientations) with corresponding selected area electron diffraction patterns from the matrix (α-Fe in the $[\bar{1}1\bar{1}]$ zone axis) and $M_{23}C_6$ carbide in 10% Cr steel.
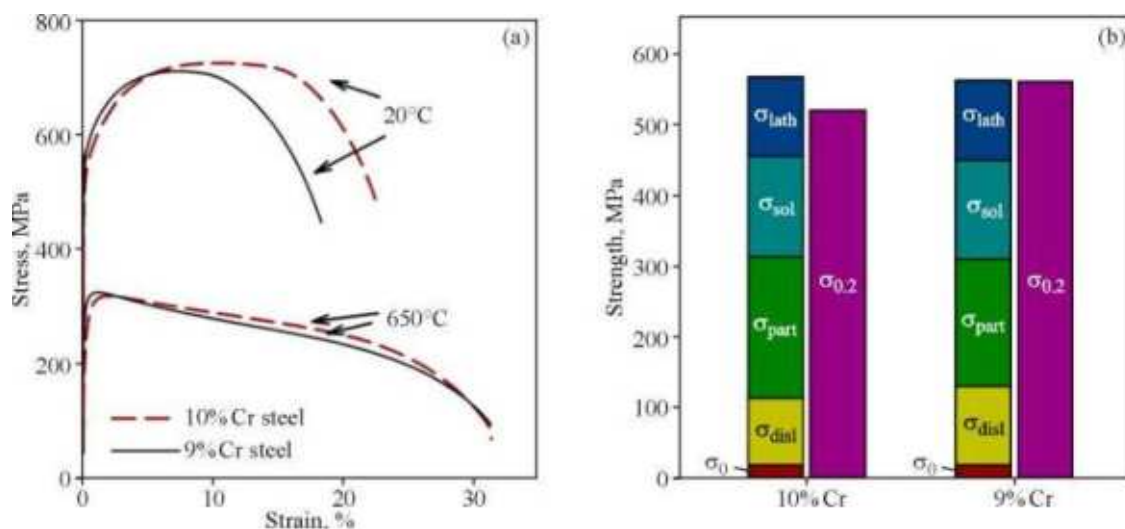
Fig. 7. Engineering stress–strain curves of 10% Cr and 9% Cr steels under uniaxial tension at room temperature and at 650°C (a); contributions of different strengthening mechanisms to the yield strength at room temperature for both steels after heat treatment (b) (color online).

main reason (together with the Laves phase) for high creep resistance in short-term tests [20].

In addition to $M_{23}C_6$ carbides, two other types of second phase particles were found in the structure of heat-treated 10% Cr steel. These are, first, round-shaped NbX carbonitride particles with an average size of 30 nm (Figs. 4a and 4c). The average chemical composition of such particles (in wt %) is 41% Nb–46% Cr–12% Fe–1% V. Their high chromium content is due to the close proximity of NbX carbonitrides to $M_{23}C_6$ carbides. The volume fraction of NbX carbonitrides was 0.054% according to Thermo-Calc calculations (Table 1). Particles of the second type are rounded M_6C carbides precipitated on $M_{23}C_6$ carbides, as previously discussed in [22], with an average size of 40 nm (Figs. 4a and 4d). The average chemical composition of these particles (in wt %) is 72% W–22% Cr–6% Fe. Their number was negligible. As shown earlier [22], M_6C particles are mainly released during creep or annealing at 650°C and serve as an intermediate phase for the formation of (Fe_2(W, Mo)) Laves phase.

3.2. Tensile Properties and Hardness. Analysis of Contributions from Various Strengthening Mechanisms

Figure 7 illustrates the room-temperature tensile behavior of 10% Cr steel versus 9% Cr steel along with the contributions of various strengthening mechanisms to the yield strength. The contributions of strengthening mechanisms were calculated as in the

previous studies [26, 27] by linear addition of the following components:

− strengthening due to lattice friction forces (Peierls forces) (σ_{part}),

− dislocation strengthening (σ_{disl}),

− dispersion strengthening from $M_{23}C_6$ carbides and MX carbonitrides (σ_{part}),

− solid solution strengthening due to substitutional elements (σ_{sol}),

− substructural strengthening from subgrains with low-angle boundaries (σ_{lath}).

The strength characteristics of 10% Cr and 9% Cr steels under uniaxial tension at room temperature and at a temperature of 650°C are close. The yield strength at 20°C is respectively 560 and 520 MPa for 9% Cr and 10% Cr steel, while the tensile strength at 20°C is 20 MPa higher for 10% Cr steel (Fig. 7a). At 650°C, the yield strength of 9% Cr steel is 1.5 times higher, and the tensile strength has the same values of 315 MPa for both steels. The relative elongation values are also close for both steels at both test temperatures.

The estimated strengthening contributions are in good agreement with the experimental yield strength. The deviation of the theoretically calculated strength value from the experimental one is less than 10% for both steels, which is comparable to the measurement error of structural parameters and yield strength. Since structural parameters such as the martensite lath width, dislocation density, and the content of Cr, W, Mo and Co in the matrix are almost the same for both steels, and rhenium in 10% Cr steels does not
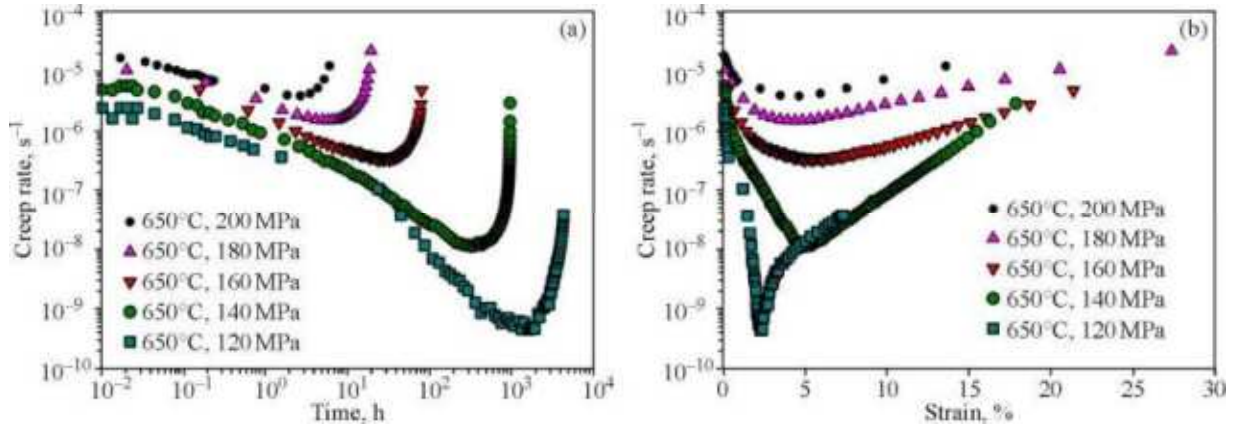
Fig. 8. Curves of creep rate versus time (a) and creep rate versus strain (b) for completed creep rupture tests at applied stresses of 200, 180, 160, 140 and 120 MPa for 10% Cr steel (color online).

contribute to solid solution strengthening, as was found earlier in [19], then the contributions of strengthening from these structural elements turn out to be comparable for 9% Cr and 10% Cr steels. The largest contribution to the yield strength comes from dispersion strengthening from second phase particles for both steels, the value of which is 180 MPa for 9% Cr steel and 200 MPa for 10% Cr steel, despite significant differences in second phase dispersions between 9% Cr and 10% Cr steels. These differences include:

– reduction in the average size of $M_{23}C_6$ carbides by 23% in 10% Cr steel at the same volume fraction of these particles in 9% Cr and 10% Cr steels,

– a 6-fold decrease in the volume fraction of MX carbonitrides in 10% Cr steel compared to 9% Cr steel as a result of nitrogen content reduction to 0.001%. The large contribution to dispersion strengthening due to the reduced size of $M_{23}C_6$ carbides in 10% Cr steel is compensated by the large volume fraction of MX carbonitrides in 9% Cr steel.

The hardness of 10% Cr and 9% Cr steels is equal to 225 ± 5 HB. These hardness values indicate that the steel has good weldability and that preheating before welding and subsequent tempering are not required [1].

3.3. Creep Resistance

Figure 8 shows plots of creep rate versus time and creep rate versus strain after creep rupture tests at applied stresses of 200, 180, 160, 140 and 120 MPa for 10% Cr steel.

The creep behavior of the studied 10% Cr steel is typical for heat-resistant martensitic steels containing dispersed second phase particles. Re-containing

10% Cr steel exhibits 3 stages of creep: primary, steady-state, and accelerated (tertiary), with the steady-state creep stage corresponding to the point of minimum creep rate. The creep rate decreases to a minimum value at low strains and then gradually increases with increasing strain. It should be noted that at lower applied nominal stresses more time is required to reach the minimum creep rate. The minimum creep rate increases from 10^{-10} to 10^{-6} s^{-1} while the applied stress increases from 120 to 200 MPa for both steels.

A comparison of the creep curves for 10% Cr and 9% Cr steels at a temperature of 650°C and applied stresses of 160, 140 and 120 MPa is presented in Fig. 9.

At an applied stress of 160 MPa, the time to rupture of 9% Cr steel increases by a factor of 6 due to a longer primary creep stage and more than an order of magnitude lower minimum creep rate compared to 10% Cr steel (Fig. 9a). At the same time, the rupture elongation of 9% Cr steel is 2 times lower than for 10% Cr steel, and the slopes of the primary and tertiary creep stages are steeper, which is indicative of active hardening at the primary stage and softening at the tertiary stage in 9% Cr steel (Fig. 9d). When reducing the applied stress to 140 MPa, the rupture time difference between the steels decreases by a factor of up to 2, which is also associated with a longer primary creep stage; the minimum creep rate of 9% Cr steel is only 2 times lower than that of 10% Cr (Fig. 9b). The rupture elongation of 9% Cr steel is also 2 times lower than for 10% Cr steel. The slopes of the tertiary stages are the same for both steels (Fig. 9e). At an applied stress of 120 MPa, the creep behavior of both steels becomes the same: the time to
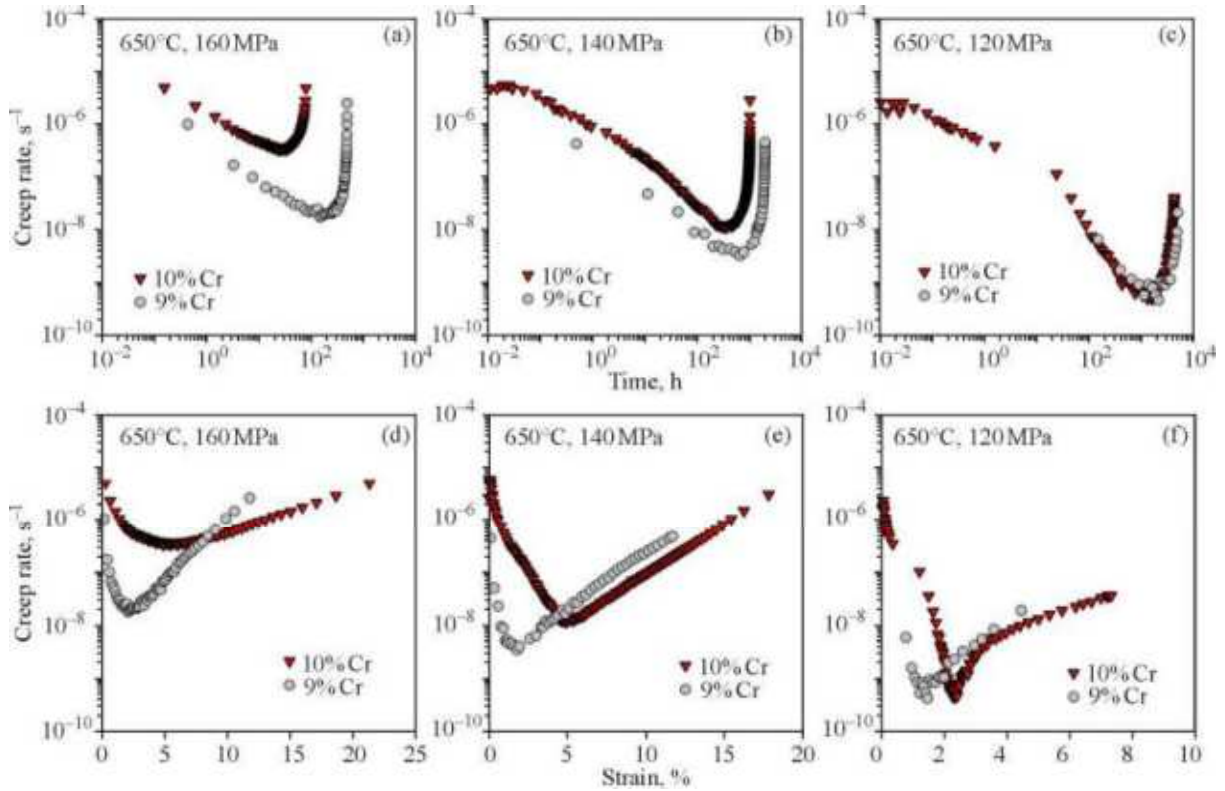
Fig. 9. Comparison of creep curves: creep rate versus time (a–c) and creep rate versus strain (d–f) for 10% Cr and 9% Cr steels at applied stresses of 160 (a, c), 140 (b, e) and 120 MPa (c, f) (color online).

rupture, the minimum creep rate, and the curve slopes at the primary and tertiary creep stages are the same (Figs. 9c and 9f). The differences include 2 times lower rupture elongation and minimum creep rate of 9% Cr steel, as was observed at higher applied stresses (Fig. 9f).

Figure 10 shows the dependence of applied stresses on time to rupture in creep rupture tests for the studied 10% Cr steel in comparison with 9% Cr steel.

As seen from Fig. 10, the rupture time of 9% Cr steel increases significantly at high applied stresses. At stresses from 200 to 160 MPa, there is a 6-fold difference in rupture time in favor of 9% Cr steel. However, the slopes of the creep rupture curves of 9% Cr and 10% Cr steels in the region of high ap-
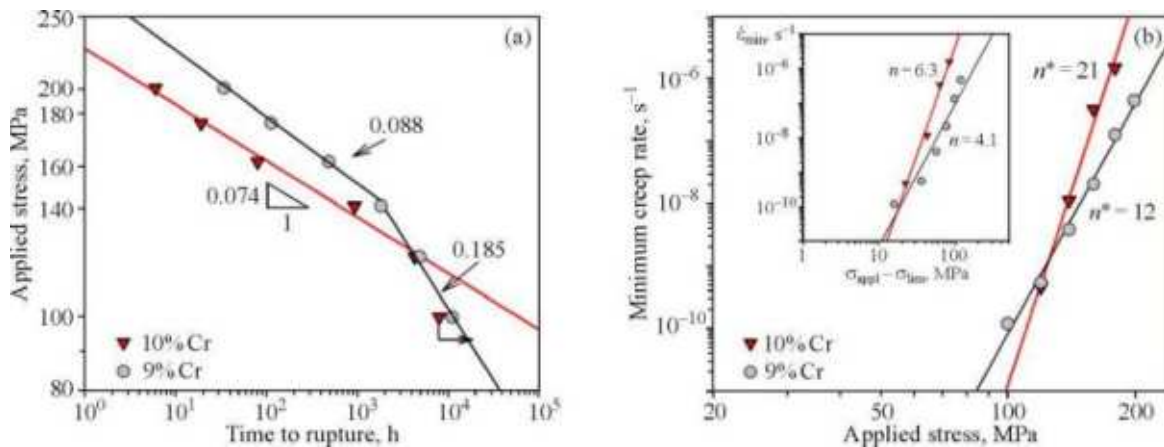

Fig. 10. Dependence of applied stress on time to rupture (a) and minimum creep rate on applied stress (b) for 10% Cr and 9% Cr steels at a test temperature of 650°C. The arrow indicates the uncompleted creep rupture test at 100 MPa, which is still ongoing at the time of writing (color online).

plied stresses are close (Fig. 10a). At an applied stress of 140 MPa, the creep rupture curve of 9% Cr steel kinks, resulting in a 2.1-times steeper slope of the curve and lower creep resistance. The curve of 10% Cr steel has no kink; all points for completed tests lie on the same straight line with a correlation coefficient of 99% (Fig. 10a). Although the studied 10% Cr steel shows low short-term creep resistance, its long-term creep resistance may not necessarily be low. The uncompleted test at 100 MPa is critical to understanding the cause of the kink in the creep rupture curve of 10% Cr steel.

The curves in Figs. 8 and 9 can be used to determine the minimum creep rate for tests conducted at a temperature of 650°C and applied stresses of 200, 180, 160, 140 and 120 MPa for the studied Re-containing 10% Cr steel in comparison with 9% Cr steel. The stress dependence of the minimum creep rate is presented in Fig. 10b, showing a linear relationship between the minimum creep rate and the applied stress. Experimental data obey the creep power law over the entire range of applied stresses in the form [1, 28]:

$$\dot{\varepsilon}_{min} = A\sigma^{n^*} \exp\left(-\frac{Q}{RT}\right), \qquad (1)$$

where $\dot{\varepsilon}_{min}$ is the minimum creep rate, σ is the applied stress, Q is the activation energy for plastic deformation, R is the gas constant, T is the temperature, A is a constant, and n^* is the "apparent" exponent.

The curve of 10% Cr steel in Fig. 10b shows the best linear fit for the "apparent" exponent in the plastic deformation equation $n^* = 21$ with a correlation coefficient of 0.98 at all applied stresses in the range of 200–120 MPa without kinks. Calculation of threshold stresses by a simple extrapolation of the curve to the X axis, corresponding to the minimum creep rate of 10^{-11} s^{-1} along the ordinate, shows that 98 MPa corresponds to the threshold stress value in 10% Cr steel. For comparison, the "apparent" exponent in the plastic deformation equation for 9% Cr steel is $n^* = 12$, and the threshold stress value is equal to 85 MPa (Fig. 10b). The creep deformation mechanism can be established from Fig. 10b that also shows the dependence of the minimum creep rate on the effective stress, defined as the difference between the applied stress and the threshold stress ($\sigma_{appl} - \sigma_{lim}$). There are four well-known cases regarding the creep behavior of materials: $n = 3$ for creep controlled by viscous glide, $n = 5$ for creep controlled by high-temperature dislocation climb (bulk diffusion), $n = 7$ for creep controlled by low-temperature dislocation
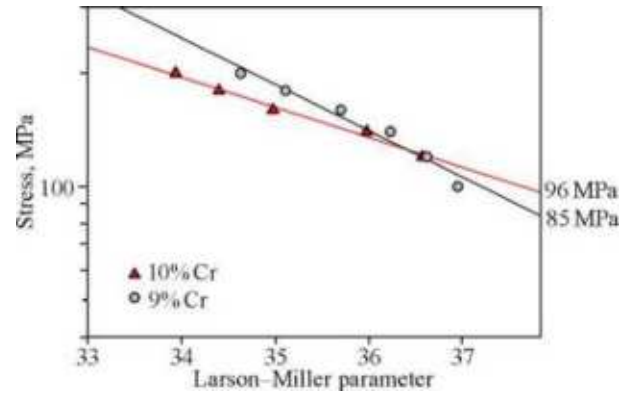

Fig. 11. Dependence of stress on the Larson–Miller parameter at a temperature of 650°C to determine the 100 000 h creep rupture strength (color online).

climb (pipe diffusion), and $n = 8$ for creep controlled by lattice diffusion with a constant structure [28]. The true stress exponent n for 10% Cr steel was 6.3 for the entire range of applied stresses, which is close to $n = 7$ and indicates creep controlled by low-temperature dislocation climb due to pipe diffusion without any change in the long-term creep deformation mechanism, while for 9% Cr steel the true stress exponent $n = 4.1$ indicates that creep in this steel is controlled by high-temperature dislocation climb due to bulk diffusion.

The creep rupture strength of 10% Cr steel in comparison with 9% Cr steel was estimated using an empirical relationship between stress and time to rupture (Larson–Miller equation):

$$P = T(\lg \tau + 36) \times 10^{-3}, \qquad (2)$$

where T is the test temperature in K, and τ is the time to rupture. Figure 11 plots the relationship between the applied stress and the Larson–Miller parameter.

The estimated 100 000 h creep rupture strength $\sigma_{10^5}^{650}$, which characterizes the creep resistance under long-term high temperature and stress conditions, for Re-containing 10% Cr steel was 96 MPa, which is 13% higher than for 9% Cr steel. Note that the creep rupture strength of commercial P92 steel is 72 MPa [29], which is almost 25% less than that of the studied Re-containing 10% Cr steel.

3.4. Microstructure after Creep

Figure 12 shows TEM and SEM micrographs of 10% Cr steel after creep rupture tests in the uniform elongation region. The structural parameters of 10% Cr steel in comparison with 9% Cr steel in the uniform deformation region (gauge part) are summa-
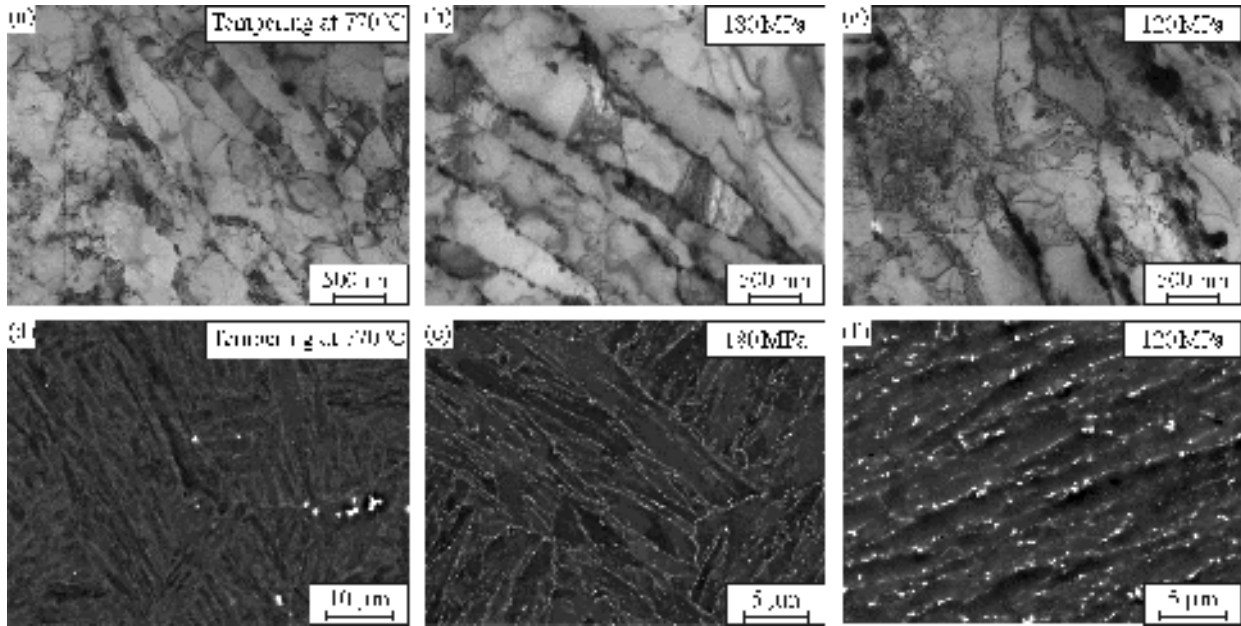
Fig. 12. Structural evolution of 10% Cr steel after creep rupture test in the uniform elongation region. TEM (a–c) and SEM (d–f).

rized in Table 3. In both steels, $(Fe_2(W, Mo))$ Laves phase particles precipitate at the high-angle boundaries of the original austenite grains, blocks and packets, as well as at the low-angle boundaries of martensite laths, which are clearly visible in the SEM Z-contrast images as white particles on gray background of the matrix (Figs. 12d–12f).

Previous studies [6, 8] showed that a large increase in lath sizes, the formation of large subgrains, a decrease in dislocation density, and a pronounced coarsening of grain boundary $M_{23}C_6$ carbides and $(Fe_2(W, Mo))$ Laves phase particles for 9% Cr steel within the uniform deformation region are observed at applied stresses below 140 MPa, which correlates with the kink in the creep rupture curve (Fig. 10a). The martensite lath width increases from 400 nm af-

ter tempering to about 1 μm in the region of low applied stresses, together with a twofold increase in the average size of second phase particles (Table 3). The dislocation density decreases by an order of magnitude compared to the initial state (Tables 2 and 3). On the contrary, for 10% Cr steel the structure remains almost unchanged at all applied stresses: the martensite lath width doubles to 600 nm, and the dislocation density decreases by a factor of 2 to 1.1×10^{14} m^{-2} (Figs. 12a–12c, Table 3). Moreover, the size of Laves phase particles and $M_{23}C_6$ carbides in 10% Cr steel remains quite small even after a creep test at 120 MPa (Fig. 12, Table 3). The smaller size of $M_{23}C_6$ carbides after testing at 160 MPa is due to the additional precipitation of particles during creep, which reduces the average size of this phase. Thus,

Table 3. Structural parameters of 10% Cr steel in comparison with 9% Cr steel after creep rupture tests in the uniform elongation region

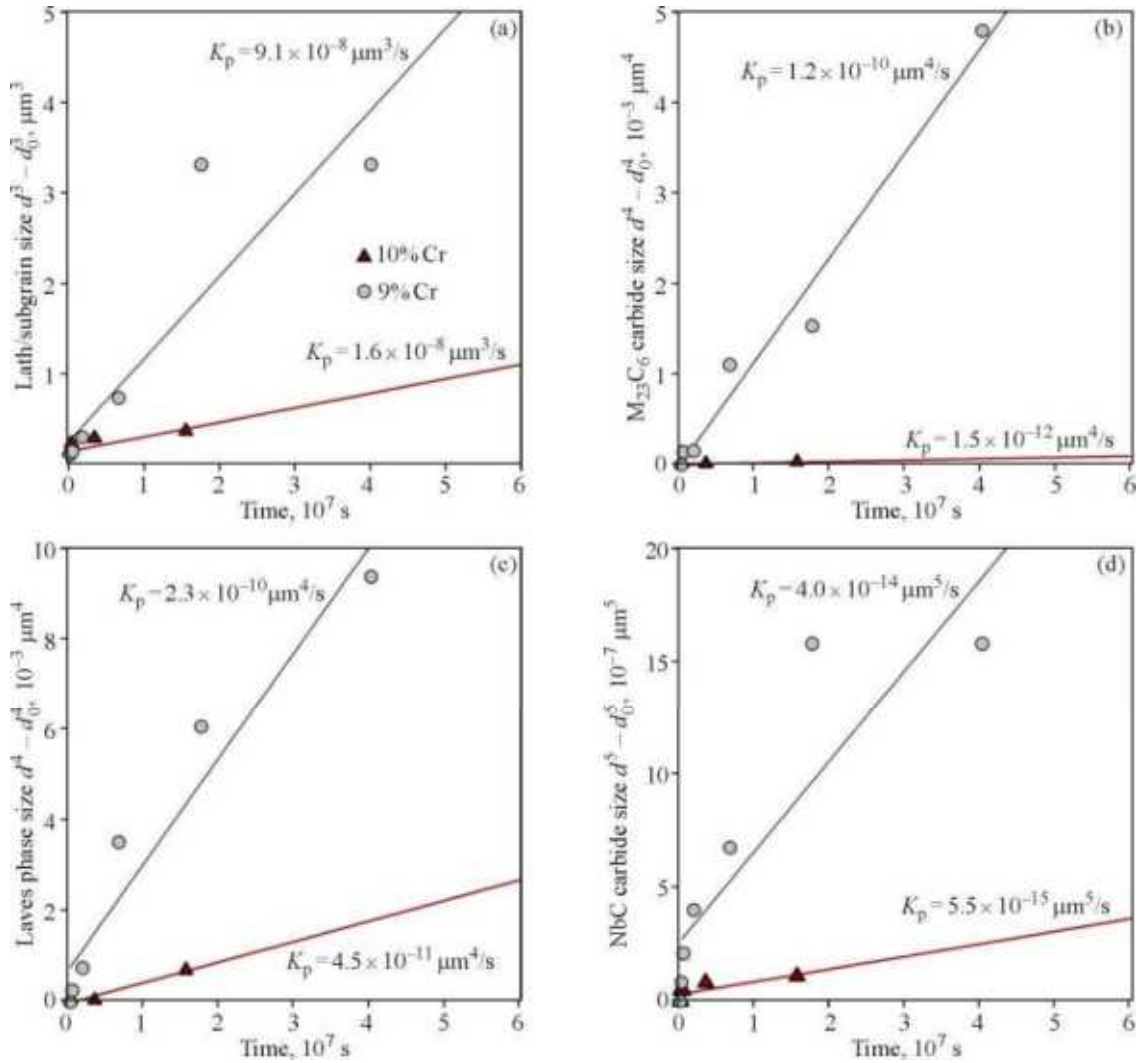| Applied stress, MPa	160		140		120	
Steel	10% Cr	9% Cr	10% Cr	9% Cr	10% Cr	9% Cr
Time to rupture, h	80	487	934	1828	4306	4869
Lath size, nm	657	720	600	930	539	–
Subgrain size, nm	–	610	631	1450	500	1500
Dislocation density, 10^{14} m^{-2}	1.7	0.4	1.13	0.2	1.1	0.1
Size of $M_{23}C_6$, nm	53	120	79	150	87	200
Size of Laves phase, nm	70	170	78	245	163	280
Size of Nb(C, N), nm	37	70	40	70	40	70

Fig. 13. Size variation of martensite laths (a) and second phase particles: $M_{23}C_6$ (b), Laves phase (c) and NbX carbon nitrides (d) in the uniform elongation region. K_p is the coarsening rate constant (color online).

the lath structure of 10% Cr steel exhibits high creep resistance over a wide range of applied stresses, which is caused by high threshold stresses (Fig. 10b).

The data obtained (Fig. 12, Table 3) indicate that the coarsening of second phase particles in the uniform elongation region occurs according to the Ostwald mechanism, described by the Lifshitz–Slyozov–Wagner equation [30, 31]:

$$d^m - d_0^m = k(t - t_0), \qquad (3)$$

where d_0 and d are respectively the average particle diameters for time t_0 and t, K is the coarsening rate constant, and the exponent n depends on the coarsening mechanism.

Coarsening of martensite laths and various second phase particles ($M_{23}C_6$ carbides, Laves phase, NbX carbonitrides) was analyzed in both steels. Figure 13

illustrates the size variation of martensite laths and second phase particles in the uniform elongation region. Coarsening rate constants of second phase particles were calculated assuming that the coarsening of martensite laths is controlled by bulk diffusion $m = 3$, the coarsening of grain boundary $M_{23}C_6$ carbides and Laves phase particles is controlled by grain boundary diffusion $m = 4$, and that of NbX carbonitrides is controlled by pipe diffusion $m = 5$.

As seen from Fig. 13, the coarsening rate of all structural elements in 10% Cr steel is much lower than in 9% Cr steel. Thus, the coarsening rate of martensite laths is 5.7 times lower in 10% Cr steel, which is accompanied by a decrease in the coarsening rate of $M_{23}C_6$ carbides by two orders of magnitude and Laves phase particles and NbX carbonitrides by an order of magnitude. Despite the same level of short-

term strength properties and the advantages of 9% Cr steel at high applied stresses, the creep resistance of high-chromium steels is determined by the magnitude of the internal threshold stress [13, 28, 32]. Threshold stresses in low-nitrogen steels are caused by coherent particles of $M_{23}C_6$ carbides along the low-angle lath boundaries, which prevent their migration during creep [13]. Thus, the higher creep rupture strength of 10% Cr steel is determined by the stability of the lath structure; the migration of lath martensite boundaries is effectively hindered by $M_{23}C_6$ carbides, whose average size remains less than 100 nm even after long-term creep tests.

4. CONCLUSIONS

A comparative analysis was performed to evaluate the mechanical properties and structure of low-nitrogen high-boron 10% Cr steel additionally alloyed with cobalt, tungsten, molybdenum and rhenium and 9% Cr steel with 0.1% carbon, 0.05% nitrogen and 0.005% boron. It was found that the long-term structural stability of martensite laths with low-angle boundaries, pinned by small $M_{23}C_6$ carbides that have orientational relationships with the matrix, becomes the key to high creep resistance under high temperature and stress conditions. The contribution of precipitation strengthening to the yield strength of 10% Cr steel is dominant among the strengthening mechanisms. The reduced contribution from MX carbonitrides is compensated by smaller $M_{23}C_6$ carbides, which play a decisive role in the structural stability of laths during creep. The 100 000 h creep rupture strength of 10% Cr steel at 650°C is equal to 96 MPa, which is 13% higher than for 9% Cr steel. In this case, the creep of 10% Cr steel is controlled by low-temperature dislocation climb due to pipe diffusion. The combination of short-term tensile properties and creep resistance of 10% Cr steel meets the requirements for unit components of thermal power plants.

CONFLICT OF INTEREST

The author of this work declares that she has no conflicts of interest.

REFERENCES

1. Abe, F., Kern, T.-U., and Viswanathan, R., *Creep-Resistant Steels*, Cambridge: Woodhead Publishing, 2008.
2. Kern, T.U., Staubli, M., and Scarlin, B., The European Efforts in Material Development for 6508C USC Power Plants—COST522, *ISIJ Int.*, 2002, vol. 242, pp. 1515–1519.
3. Klueh, R.L., Elevated-Temperature Ferritic and Martensitic Steels and Their Application to Future Nuclear Reactors, *Int. Mater. Rev.*, 2005, vol. 50, pp. 287–310. https://doi.org/10.1179/174328005X41140
4. Bladesha, H.K.D.H., Design of ferritic creep-resistant steels, *ISIJ Int.*, 2001, vol. 41, pp. 626–640. https://doi.org/10.2355/isijinternational.41.626
5. Kaybyshev, R.O., Skorobogatykh, V.N., and Shchenkova, I.A., New Martensitic Steels for Fossil Power Plant: Creep Resistance, *Phys. Met. Metallogr.*, 2010, vol. 109, pp. 186–200. https://doi.org/10.1134/S0031918X10020110
6. Fedoseeva, A., Nikitin, I., Tkachev, E., Mishnev, R., Dudova, N., and Kaibyshev, R., Effect of Alloying on the Nucleation and Growth of Laves Phase in the 9–10% Cr–3% Co Martensitic Steels during Creep, *Metals*, 2021, vol. 11, p. 60. https://doi.org/10.3390/met11010060
7. Maruyama, K., Sawada, K., and Koike, J., Strengthening Mechanisms of Creep Resistant Tempered Martensitic Steel, *ISIJ Int.*, 2001, vol. 41, pp. 641–653. https://doi.org/10.2355/isijinternational.41.641
8. Fedoseeva, A., Dudova, N., and Kaibyshev, R., Creep Strength Breakdown and Microstructure Evolution in a 3% Co Modified P92 Steel, *Mater. Sci. Eng. A*, 2016, vol. 654, pp. 1–12. https://doi.org/10.1016/j.msea.2015.12.027
9. Dronhofer, A., Pešička, J., Dlouhy, A., and Eggeler, G., On the Nature of Internal Interfaces in Tempered Martensite Ferritic Steels, *Mater. Res. Adv. Tech.*, 2003, vol. 94, pp. 511–520. https://doi.org/10.1515/ijmr-2003-0091
10. Kostka, A., Tak, K.-G., Hellmig, R.J., Estrin, Y., and Eggeler, G., On the Contribution of Carbides and Micrograin Boundaries to the Creep Strength of Tempered Martensite Ferritic Steels, *Acta Mater.*, 2007, vol. 55, pp. 539–550. https://doi.org/10.1016/j.actamat.2006.08.046
11. Abe, F., Effect of Fine Precipitation and Subsequent Coarsening of Fe_2W Laves Phase on the Creep Deformation Behavior of Tempered Martensitic 9Cr-W Steels, *Metall. Trans. A*, 2005, vol. 36, pp. 321–332. http://doi.org/10.1007/s11661-005-0305-y

12. Prat, O., Garcia, J., Rojas, D., Sauthoff, G., and In-den, G., The Role of Laves Phase on Microstructure Evolution and Creep Strength of Novel 9% Cr Heat Resistant Steels, *Intermetallics*, 2013, vol. 32, pp. 362–372. https://doi.org/10.1016/j.intermet.2012.08.016

13. Fedoseeva, A., Tkachev, E., and Kaibyshev, R., Advanced Heat-Resistant Martensitic Steels: Long-Term Creep Deformation and Fracture Mechanisms, *Mater. Sci. Eng. A*, 202, vol. 862, p. 144438. https://doi.org/10.1016/j.msea.2022.144438

14. Abe, F., Taneike, M., and Sawada, K., Alloy Design of Creep Resistant 9Cr Steel Using a Dispersion of Nano-Sized Carbonitrides, *Int. J. Press. Vessel. Pip.*, 2007, vol. 84, pp. 3–12. https://doi.org/10.1016/j.ijpvp.2006.09.003

15. Horiuchi, T., Igarashi, M., and Abe, F., Improved Utilization of Added B in 9Cr Heat-Resistant Steels Containing W, *ISIJ Int.*, 2002, vol. 42, pp. 67–71. https://doi.org/10.2355/isijinternational.42.Suppl_S67

16. Abe, F., Effect of Boron on Microstructure and Creep Strength of Advanced Ferritic Power Plant Steels, *Proc. Eng.*, 2011, vol. 10, pp. 94–99. https://doi.org/10.1016/j.proeng.2011.04.018

17. Viswanathan, R. and Bakker, W., Materials for Ultra-supercritical Coal Power Plants—Turbine Materials: Part 2, *J. Mater. Eng. Perform.*, 2001, vol. 10, pp. 96–101. https://doi.org/10.1361/105994901770345394

18. Fukuda, M., Tsuda, Y., Yamashita, K., Shinozaki, Y., and Takanashi, T., Materials and Design for Advanced High Temperature Steam Turbines, in *Conf. Proc. Advances in Materials Technology for Fossil Power Plants, 25–28 Oct. 2004, Hilton Head Island, South Carolina*, Viswanathan, R., Gandy, D., and Coleman, K., Eds., Materials Park: ASM Int., 2005, pp. 491–505.

19. Fedoseeva, A., Nikitin, I., Dudova, N., and Kaibyshev, R., On Effect of Rhenium on Mechanical Properties of a High-Cr Creep Resistant Steel, *Mater. Lett.*, 2019, vol. 269, pp. 81–84. https://doi.org/10.1016/j.matlet.2018.10.081

20. Fedoseeva, A., Nikitin, I., Dudova, N., and Kaibyshev, R., Superior Creep Resistance of a High-Cr Steel with Re Additives, *Mater. Lett.*, 2020, vol. 262, p. 127183. https://doi.org/10.1016/j.matlet.2019.127183

21. Fedoseeva, A., Nikitin, I., Dudova, N., and Kaibyshev, R., Strain and Temperature Contributions to Structural Evolution in a Re-Containing 10% Cr–3% Co–3% W Steel during Creep, *Mater. High Temp.*, 2021, vol. 38, pp. 237–246. https://doi.org/10.1080/09603409.2021.1924548

22. Fedoseeva, A., Nikitin, I., Dudova, N., and Kaibyshev, R., Nucleation of W-Rich Carbides and Laves Phase in a Re-Containing 10% Cr Steel during Creep at 650°C, *Mater. Char.*, 2020, vol. 169, p. 110651. https://doi.org/10.1016/j.matchar.2020.110651

23. Humphreys, F.J. and Hatherly, M., *Recrystallization and Related Annealing Phenomena*, New York: Elsevier, 2004.

24. Fedoseeva, A., Dolzhenko, A., and Kaibyshev, R., Thermo-Mechanical Processing as Method Decreasing Delta-Ferrite and Improving the Impact Toughness of the Novel 12% Cr Steels with Low N and High B Contents, *Materials*, 2022, vol. 15, p. 8861. https://doi.org/10.3390/ma15248861

25. Kipelova, A., Odnobokova, M., Belyakov, A., and Kaibyshev, R., Effect of Co on Creep Behavior of a P911 Steel, *Metall. Mater. Trans A*, 2013, vol. 44, pp. 577–583. https://doi.org/10.1007/s11661-012-1390-3

26. Fedoseeva, A., Dudko, V., Dudova, N., and Kaibyshev, R., Effect of Co on the Strengthening Mechanisms of the Creep-Resistant 9% Cr–2% W–MoVNb Steel, *J. Mater. Sci.*, 2022, vol. 57, pp. 21491–21501. https://doi.org/10.1007/s10853-022-07940-z

27. Nikitin, I., Fedoseeva, A., and Kaibyshev, R., Strengthening Mechanisms of Creep-Resistant 12% Cr–3% Co Steel with Low N and High B Contents, *J. Mater. Sci.*, 2020, vol. 55, pp. 7530–7545. https://doi.org/10.1007/s10853-020-04508-7.

28. Spigarelli, S., Cerri, E., Bianchi, P., and Evangelista, E., Interpretation of Creep Behavior of a 9Cr–Mo–Nb–V–N (T91) Steel Using Threshold Stress Concept, *Mater. Sci. Technol.*, 1999, vol. 15, pp. 1433–1440. https://doi.org/10.1179/026708399101505428

29. Vallourec & Mannesmann Tubes, in *T92/P92 Steel Handbook. (Ultra-) Supercritical Boiler Steel and Welding Technical Symposium*, 2005, vol. 3, pp. 285–304.

30. Wagner, C., Theorie der Alterung von Niederschlaegen durch Umlosen (Ostwald Reifung), *Phys. Chem. Chem. Phys.*, 2010, vol. 65, pp. 581–591. https://doi.org/10.1002/BBPC.19610650704

31. Lifshitz, M. and Slyozov, V.V., The Kinetics of Precipitation from Supersaturated Solid Solutions, *J. Phys. Chem. Solids*, 1961, vol. 19, pp. 35–50. https://doi.org/10.1016/0022-3697(61)90054-3

32. Dudova, N., Mishnev, R., and Kaibyshev, R., Creep Behavior of a 10% Cr Heat-Resistant Martensitic Steel with Low Nitrogen and High Boron Contents at 650°C, *Mater. Sci. Eng. A*, 2019, vol. 766, p. 138353. https://doi.org/10.1016/j.msea.2019.138353